Aerospace Science and Technology 156 (2025) 109755

Contents lists available at ScienceDirect

Aerospace Science and Technology

journal homepage: www.elsevier.com/locate/aescte

Autonomous numerical predictor-corrector guidance for human Mars landing missions

Youngro Lee, David D. Lee *, Bong Wie

Department of Aerospace Engineering, Iowa State University, 537 Bissell Rd, Ames, 50011, IA, USA

ARTICLE INFO

Communicated by Amit Kumar Sanyal

Keywords:
Mars entry descent and landing
Entry guidance
Numerical predictor-corrector
Bank angle parameterization

ABSTRACT

The numerical predictor-corrector guidance method with a linear bank angle parameterization has been widely applied to various atmospheric entry guidance problems. However, it has been found that the linear bank angle approach has limitations in satisfying the final state requirement of a specific type of atmospheric entry mission. In response, this paper proposes a novel bank angle parameterization based on a logistic function, which improves the energy preservation capability and increases the potential final altitude at the end of the entry phase. The paper also suggests a guideline to determine a guidance law activation point for better entry performance. Numerical simulations demonstrate that the proposed guidance scheme outperforms the linear bank profile approach and is suitable for future human Mars landing missions.

1. Introduction

A numerical predictor-corrector (NPC) technique has been widely researched in atmospheric entry guidance applications, such as 1) Mars Entry, Descent, and Landing (EDL) system [1], 2) aerocapture for orbital insertion [2], 3) Hypersonic Gliding Vehicle (HGV) [3], and 4) reentry of the Reusable Launch Vehicle (RLV) [4]. The NPC targeting guidance algorithm was originally developed at NASA Langley Research Center for the Mars Surveyor Program (MSP) 2001 mission [2,5]. Unfortunately, the MSP 2001 mission was canceled and later reborn as Phoenix in 2003, yet NPC was not implemented because the high-accuracy landing was unnecessary for the Phoenix mission [6].

NASA has successfully landed nine Mars landers to date, with only two employing a guided entry phase for precision landing: the Mars Science Laboratory [7] and the Perseverance Mars Rover [8]. Although over fifty years have passed since the completion of Apollo re-entry missions, a modified version of the Apollo heritage has been used for their Mars EDL phases. The Apollo final phase entry guidance utilizes a reference path-planning and tracking scheme, and bank angle commands are generated to track altitude rate and drag profiles along the entry trajectory [9]. Because the capability and applicability of the NPC targeting guidance algorithm have been proven by many research works, it is now being considered a candidate to be used for a future human Mars landing mission [10]. NASA currently aims to send humans to Mars in the 2030s, and relevant research is actively ongoing [11].

Most Mars robotic landing missions have used parachutes to slow down and prepare for landing. To successfully deploy the parachute, the entry phase must end within a specific velocity-altitude boundary, known as the parachute deployment box or envelope [12–14]. A minimum altitude of 6 km above the ground, or more than 8 km preferred, was found for the parachute deployment of the MSL mission [7]. In contrast to robotic missions, it's unlikely that supersonic parachutes would be feasible for a human-scale Mars landing mission [15]. As a result, employing a Supersonic RetroPropulsion (SRP) system right after the atmospheric entry phase becomes necessary, which requires a predetermined set of velocity and altitude at the end of an entry trajectory [11,16,17]. Therefore, the entry guidance for the human-scale Mars landing mission should consider the technical challenge of safely and precisely decelerating a vehicle weighing approximately 58.7 metric tons. Entry trajectory comparisons between the Mars robotic and human-scale landing missions are presented in our previous studies [18,19].

The numerical predictor-corrector guidance (NPCG) algorithm can provide high targeting accuracy in the presence of dispersions and randomness because it directly utilizes nonlinear dynamics to predict the entry vehicle's motion. In particular, the effectiveness of the NPCG can be attributed to the bank angle parameterization. By assuming the bank angle profile in a specific shape, the highly nonlinear entry guidance problem can be solved efficiently onboard. In 2003, DiCarlo [20] proposed using a constant bank angle profile in the NPCG algorithm for an aerocapture guidance system to ensure re-entry into Earth. In the

* Corresponding author.
E-mail addresses: youngro@iastate.edu (Y. Lee), daylee@iastate.edu (D.D. Lee), bongwie@iastate.edu (B. Wie).

https://doi.org/10.1016/j.ast.2024.109755
Received 24 March 2024; Received in revised form 30 September 2024; Accepted 17 November 2024
Available online 20 November 2024

Nomenclature

β	ballistic coefficient
$\mathcal{E}$	conventional specific energy
$\dot{Q}$	aerodynamic heating rate
γ	relative flight path angle
μ	Mars gravitational parameter
ω	Mars spin rate
ϕ	latitude
ϕ_0	initial latitude
ϕ_t	target latitude
ψ	relative heading angle
ρ	air density
σ	bank angle
σ_0	initial bank angle
σ_f	final bank angle
σ_{cmd}	bank angle command
θ	longitude
θ_0	initial longitude
θ_t	target longitude
A	gravity loads
C_D	drag coefficient
C_L	lift coefficient
D	drag acceleration
d	great circle distance
e	energy-like variable
e_0	initial energy-like value
e_f	final energy-like value
e_{ga}	energy-like value at guidance activation
g	gravitational acceleration
h	geocentric altitude
h_t	target altitude
K	decay rate
L	lift acceleration
L/D	lift-over-drag ratio
m	entry vehicle mass
q	dynamic pressure
r	radial distance
R^C	crossrange
R^D	downrange
R^D_{go}	downrange-to-go
R_{go}	range-to-go
S	entry vehicle reference area
s	distance traveled
s_f	current range-to-go
T_a	air temperature
t_{ga}	guidance activation time
V	relative velocity
V_t	target velocity
z	terminal range error

same year, Zimmerman proposed using a linear bank angle profile as a function of time to develop a guidance system for a reusable launch vehicle [21]. In 2007, Joshi utilized the linear bank angle parameterization along with the angle of attack parameterization to generate feasible entry trajectories [22].

Numerous entry guidance algorithms based on the NPC technique have been developed, and among those, a series of works by Lu has contributed significantly to the relevant research and received much attention. In 2008, Lu started using the linear bank angle parameterization to solve planetary atmospheric entry problems [23]. To enforce common inequality constraints of entry trajectories in the NPCG framework, they utilized the so-called quasi-equilibrium-glide condition to translate the path constraints into bank angle magnitude limits [24]. Moreover, the outstanding performance of the NPCG in achieving an accurate landing was demonstrated by comparing it with the Apollo skip entry guidance [25]. Eventually, a unified predictor-corrector entry guidance method was developed, capable of being used with a wide range of entry vehicles and mission types [26]. They named the proposed guidance method fully numerical predictor-corrector entry guidance (FNPEG), and its capability, strong robustness, and excellent performance in the presence of high dispersions and uncertainties were further demonstrated when compared to PredGuid, which is the entry guidance system for the Orion spacecraft [27]. This paper utilizes the baseline NPCG algorithm combined with the linear bank angle parameterization discussed in Lu's publications.

Although the linear bank angle parameterization-based numerical predictor-corrector guidance (LNPCG) has been studied extensively in many research works, this paper aims to show its limitations and propose a way to resolve the issue. It has been claimed that the use of linear bank angle parameterization can reserve sufficient energy margins toward the end of the entry trajectory and achieve a desired final state [23]. However, when the LNPCG is used in a future human mission to Mars, the linear bank angle tends to result in a faster energy dissipation rate than intended. As a result, the final condition may not be met.

In our previous study [18], the LNPCG was compared with other guidance methods primarily in terms of the final states of entry trajectories. To compare the final velocity, a numerical propagation of the NPCG algorithm in the energy domain was set to cease when an entry vehicle reaches a predefined final altitude instead of a final energy. Although this approach didn't deteriorate the ability to satisfy final range constraints, it considerably increased the final velocity. Given the primary objective of minimizing fuel consumption during the powered descent phase, which is a subsequent phase in the human Mars missions, the method employed in the previous work was merely a stopgap. The proposed method in this paper addresses the drawback of the LNPCG algorithm directly without increasing the final velocity.

Various bank angle parameterizations have been proposed to improve the limited capability of the LNPCG. The work in [28] suggested an exponential decaying bank angle parameterization to prevent control saturation during the entry flight. They found that exponential decay preserves more control authority in the late entry phase compared to constant or linear bank angle assumptions. In [29], the authors aimed to alleviate gravity loads (g-load) by employing a segmented bank angle parameterization: linear in the first and last segments and constant in the middle. By implementing a low-magnitude bank command where the g-load peak occurs, they successfully suppressed the g-load peaks. In [30], the authors recognized that the constant or the linear bank angle parameterizations could lead to a final altitude mismatch. To enhance the ability to adjust the bank angle profile and meet the final altitude constraint, they proposed a piecewise linear bank angle profile with two fixed initial and final bank angles, while the NPC technique determines the middle point bank angle. The authors in [31] developed a predictor-corrector guidance method for entry missions involving waypoints and no-fly zones. They divided the entry phase into the initial and glide phases and used a piecewise linear function to parameterize the bank angle, which allowed them to satisfy the mission constraints.

This paper demonstrates that the linear bank angle parameterization employed in the LNPCG has a limited capability to preserve sufficient energy toward the end of entry trajectories. Comprehensive simulations indicate that when applied in a future human Mars entry mission, the LNPCG tends to produce lower final altitudes than required, which could lead to a ground collision. To address this issue, a novel bank angle parameterization that uses a logistic function instead of a linear function is proposed while maintaining the baseline NPCG algorithm. The pro-

posed guidance scheme aims to reduce energy dissipation rates during the early entry phase by improving the flexibility of the bank angle profile.

The advantage of the entry guidance method to be proposed here is simplicity. The aforementioned studies in which various NPCG methods were introduced often require intricate processes. Our approach can overcome the limitation of the linear bank angle parameterization without increasing the complexity of the guidance algorithm. Additionally, a guideline is suggested for determining the activation time of the guidance law that can maximize energy preservation in the early entry phase. Therefore, by simply replacing the bank angle parameterization and carefully selecting guidance activation time, a satisfactory entry trajectory for future human Mars missions can be achieved. The proposed guidance scheme is called autonomous numerical predictor-corrector guidance (ANPCG).

The contributions of this paper are summarized as follows. Firstly, the limited applicability of the linear bank angle parameterization is revealed through comprehensive numerical simulations. Secondly, an entry guidance method based on a novel bank angle parameterization is developed for a future human Mars entry mission, and its performance is demonstrated. Lastly, a new stopping criterion for the numerical predictor-corrector guidance algorithm is suggested, and its stability is demonstrated.

The remainder of the paper is structured as follows: Section 2 outlines the Mars atmospheric entry guidance problem. Section 3 describes the LNPCG algorithm and demonstrates its limited capability through comprehensive simulation analysis. Section 4 proposes our entry guidance law that resolves the issue of the LNPCG. Finally, Section 5 concludes the paper and suggests potential research items.

2. Problem formulation

2.1. Equations of motion

The three degree-of-freedom (DOF) equations of motion of an entry vehicle with respect to the spherical Mars-centered-rotating (MCR) and the north-east-down (NED) reference frames, which are shown in Fig. 1, are given by [18]

$$\dot{r} = V\sin\gamma \tag{1a}$$

$$\dot{\theta} = \frac{V\cos\gamma\sin\psi}{r\cos\phi} \tag{1b}$$

$$\dot{\phi} = \frac{V\cos\gamma\cos\psi}{r} \tag{1c}$$

$$\dot{V} = -D - g\sin\gamma + \omega^2 r\cos\phi\,(\sin\gamma\cos\phi - \cos\gamma\sin\phi\cos\psi) \tag{1d}$$

$$\dot{\gamma} = \frac{L\cos\sigma}{V} + \left(\frac{V}{r} - \frac{g}{V}\right)\cos\gamma + 2\omega\cos\phi\sin\psi + \frac{\omega^2 r}{V}\cos\phi\,(\cos\gamma\cos\phi + \sin\gamma\sin\phi\cos\psi) \tag{1e}$$

$$\dot{\psi} = \frac{L\sin\sigma}{V\cos\gamma} + \frac{V}{r}\cos\gamma\sin\psi\tan\phi + 2\omega\,(\sin\phi - \tan\gamma\cos\phi\cos\psi) + \frac{\omega^2 r}{V\cos\gamma}\sin\phi\cos\phi\sin\psi \tag{1f}$$

where r is the radial distance from the center of Mars; θ is the longitude measured from the prime meridian; ϕ is the latitude measured from the equator; V is the relative ground velocity of the entry vehicle to the rotating Mars surface; γ is the relative flight-path angle measured from the local horizontal plane; ψ is the relative heading (or azimuth) angle measured from the north in a clockwise direction; ω is the Mars spin rate; and σ is the bank angle defined as positive for turn to the right.

The gravitational, lift, and drag accelerations are respectively described by

$$g = \frac{\mu}{r^2} \tag{2a}$$

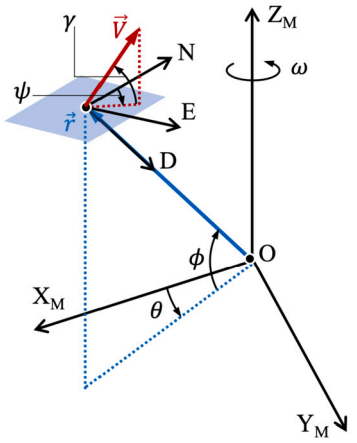

Fig. 1. The Mars-centered-rotating (MCR) and the north-east-down (NED) frames [18].

$$L = \left(\frac{1}{2}\rho V^2\right)\frac{C_L S}{m} \tag{2b}$$

$$D = \left(\frac{1}{2}\rho V^2\right)\frac{C_D S}{m} \tag{2c}$$

where μ is the gravitational parameter of Mars, C_L and C_D are the lift and drag coefficients, and S and m are the cross-sectional reference area and mass of an entry vehicle, respectively. These five parameters are assumed to be constant, and a uniform gravity model is utilized. The ballistic coefficient of the entry vehicle is defined as

$$\beta = \frac{m}{C_D S} \tag{3}$$

The angle of attack is assumed to be held constant so that the lift-over-drag ratio L/D remains constant for this study.

The range denoted as s indicates the flight distance traveled from the entry interface to the current location such that

$$\dot{s} = V\cos\gamma \tag{4}$$

Since the range s monotonically increases as an entry vehicle approaches a target destination, it is often adopted as a state variable for range control guidance methods [26,32,33].

2.2. Entry path constraints

A guidance system should monitor and handle the entry path constraints such as g-load A, dynamic pressure q, and aerodynamic heating rate $\dot{Q}$, which are defined as

$$A = \sqrt{L^2 + D^2} \le A_{max} \tag{5a}$$

$$q = \frac{1}{2}\rho V^2 \le q_{max} \tag{5b}$$

$$\dot{Q} = k\rho^N V^M \le \dot{Q}_{max} \tag{5c}$$

where the subscript "max" indicates the allowable limits for each quantity. G-load and dynamic pressure are associated with the safety of payloads, entry vehicle design, and astronauts. As L/D and β are assumed as constant in this study, A and q have a proportional relationship. The heating rate $\dot{Q}$ is governed by the thermal protection system of entry vehicles, and the parameters in the heat flux model are assumed as $N = 0.5$, $M = 3.15$, and $k = 5.3697 \times 10^{-5}$ [34]. Note that this study does not discuss path constraint handling methods. Instead, different peak levels in the path constraints led by different guidance methods are presented and compared.

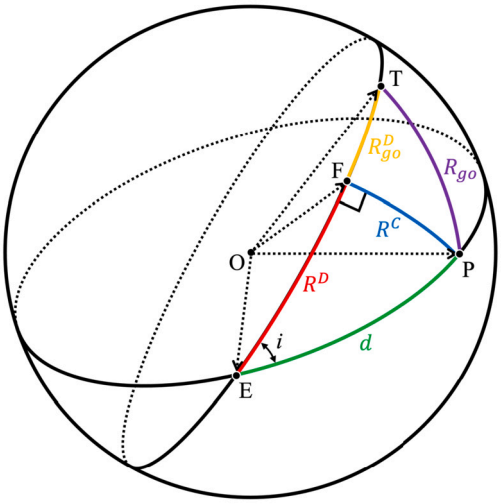

Fig. 2. Spherical trigonometry applied to the planetary entry problem [18].

2.3. Distance measures

Fig. 2 shows a unit sphere in which the initial entry, current, and target locations of the entry vehicle are denoted as $E\left(\theta_0, \phi_0\right)$, $P\left(\theta, \phi\right)$, and $T\left(\theta_t, \phi_t\right)$, respectively. The crossrange R^C and downrange R^D in units of radians can be calculated by using the relationships between arcs and angles of a spherical polygon defined by intersecting great circles as follows:

$$R^C = \sin^{-1}\left(\sin i \ \sin d\right) \tag{6a}$$

$$R^D = \cos^{-1}\left(\frac{\cos d}{\cos R^C}\right) \tag{6b}$$

where the great circle distance d, in units of radians, between two points E and P is computed as

$$d = \cos^{-1}\left(\sin\phi_0 \sin\phi + \cos\phi_0 \cos\phi \cos\left(\theta - \theta_0\right)\right) \tag{7}$$

The angle i, represented with a double-headed arrow in Fig. 2, is measured using a set of normal vectors as

$$i = \cos^{-1}\left(\hat{n}_{OEP} \cdot \hat{n}_{OET}\right) \tag{8}$$

where the normal vectors are defined as

$$\hat{n}_{OEP} = \frac{\hat{r}_{OE} \times \hat{r}_{OP}}{\|\hat{r}_{OE} \times \hat{r}_{OP}\|} \tag{9a}$$

$$\hat{n}_{OET} = \frac{\hat{r}_{OE} \times \hat{r}_{OT}}{\|\hat{r}_{OE} \times \hat{r}_{OT}\|} \tag{9b}$$

We introduce the downrange-to-go, denoted as R^D_{go}, which corresponds to the arc $\widehat{FT}$, to express the missed distance in the longitudinal direction only. Note that the range-to-go R_{go} is a combination of the downrange-to-go R^D_{go} and the crossrange R^C, as shown in Fig. 2.

The crossrange R^C can have either positive or negative value depending on the entry vehicle's location with respect to the great-circle line that connects the initial and target locations ($\widehat{ET}$ in Fig. 2). Equivalently, the sign of crossrange can be determined by the relationship between a set of normal vectors in the unit sphere. If an entry vehicle is flying on the right side of $\widehat{ET}$, the following holds:

$$\frac{\hat{n}_{OEP} \times \hat{n}_{OET}}{\|\hat{n}_{OEP} \times \hat{n}_{OET}\|} \cdot \hat{r}_{OE} > 0 \tag{10}$$

In the case of the entry vehicle flying left side of $\widehat{ET}$, the sign of Eq. (10) becomes negative.

The heading angle error $\Delta\psi$ measures the misalignment of the entry vehicle's velocity direction with respect to the target.

Table 1
Human Mars atmospheric entry mission.

	Symbols	Values
Entry Interface [35]	h_0	125 km
	θ_0	-176.40167 deg
	ϕ_0	-21.3 deg
	V_0	4700 m/s
	γ_0	-10 deg
	ψ_0	-2.8758 deg
Final Condition [35]	θ_t	-175.8 deg
	ϕ_t	0.276 deg
	V_t	450 m/s
	h_t	2480 m
Targeting Accuracy Requirement [39]	$R_{go}(t_f)$	$\leq$ 5 km
Initial Range-to-go	$R_{go}(t_0)$	1279.4 km
Entry Vehicle Aerodynamic Property [11]	L/D	0.54
	β	379 kg/m^2
Path Constraints Requirements [16]	A	$\leq$ 4 g
	q	$\leq$ 13 kPa
	$\dot{Q}$	$\leq$ 500 kW/m^2

$$\Delta\psi = \text{sgn}\{(\hat{V}_p \times \hat{\Delta}_p) \cdot \hat{r}\} \cos^{-1}(\hat{V}_p \cdot \hat{\Delta}_p) \tag{11}$$

where $\hat{V}_p$ and $\hat{\Delta}_p$ represent the target pointing vector and the velocity vector, respectively, which are projected onto the local horizontal plane and normalized, as follows:

$$\hat{V}_p = \begin{bmatrix} -\sin\psi \sin\theta - \cos\psi \cos\theta \sin\phi \\ \cos\theta \sin\psi - \cos\psi \sin\phi \sin\theta \\ \cos\phi \cos\psi \end{bmatrix}^{MCR} \tag{12}$$

$$\hat{\Delta}_p = \{\hat{r} \times \left(\hat{r}_t - \hat{r}\right)\} \times \hat{r} \tag{13}$$

where $\hat{r}$ and $\hat{r}_t$ refer to the unit position vectors of the entry vehicle and the target location in the MCR frame.

2.4. Human Mars atmospheric entry mission

The entry guidance example mainly addressed in this paper is a future human Mars mission currently under development by NASA. As specific details, including the entry interface state, have not been fully determined, the entry example is formulated based on information available in several publications such as Refs. [17,34–38]. The entry vehicle is called the Cobra Mid lift-to-drag ratio Rigid Vehicle (CobraMRV), which utilizes an aero-propulsive control strategy, including aero-surfaces and Reaction Control System (RCS) thrusters. Table 1 provides a set of the numerical data of a reference mission model studied in this paper. Note that the entry interfaces and target locations are given in the MCR and NED frames.

As mentioned in the introduction section, the entry phase for the human-scale Mars landing mission can be more challenging than robotic missions. Most Mars rover missions deploy parachutes at an altitude of 6–8 km, but for a human-scale mission, the entry phase should end closer to the ground, at around 3 km, which enables a more fuel-efficient maneuver for the powered descent landing phase. As a result, the entry guidance for the human Mars landing mission needs to be flexible to accommodate a wide range of final altitudes.

The Martian air density model in [40] is adopted for the simulation study here, which is given by

$$\rho(h) = \rho_0 \exp\left(-0.000105h\right) \tag{14}$$

where h is the altitude in units of kilometers from the Martian surface, and the reference air density ρ_0 is a function of temperature T_a with two constants $\alpha_1 = 559.35$ and $\alpha_2 = 188.95$ as

$$\rho_0 = \frac{\alpha_1}{\alpha_2 T_a} \tag{15}$$

where

$$T_a = 1.4 \times 10^{-13} h^3 - 8.85 \times 10^{-9} h^2 - 1.245 \times 10^{-3} h + 205.36 \tag{16}$$

Some parameters used in the simulations are: the Mars gravitational parameter μ is 42828 km^2/s^2, the Mars radius r_m is 3397 km, and the Mars spin rate ω is 7.088×10^{-5} rad/s. The simulations are conducted using MATLAB® R2022a on a MacBook Pro with 2.6 GHz 6-core Intel Core i7 and 16 GB of DDR4 RAM. MATLAB's ODE45 is used as a numerical integrator.

2.5. Bank control constraints

The CobraMRV flight control system uses RCS thrusters and aerosurfaces to control the attitude. To test the feasibility of a human mission to Mars, the control system's ability to track guidance commands was evaluated in Ref. [17]. The study found that the best performance was achieved with bank rate limits of 15 deg/s and higher. Another study, Ref. [36], constrained bank maneuvers with an acceleration limit of 5 deg/s^2 and a rate limit of 20 deg/s. Nonetheless, the simulation framework presented in this paper does not take into account the magnitude and rate constraints on the bank angle control, i.e., guidance commands are directly applied to the dynamic model without any attitude control latency. We aim to clearly identify the performance difference between the two entry guidance methods by excluding any other factors that might affect the guidance performance. Furthermore, the simplicity of the framework allows any readers of interest to duplicate the simulation results found here.

3. Linear bank profile-based numerical predictor-corrector guidance (LNPCG)

This section describes the LNPCG algorithm and demonstrates its limited capability when applied to the human Mars atmospheric entry mission.

3.1. LNPCG algorithm description

The LNPCG algorithm seeks a parameterized bank angle profile for the longitudinal trajectory from the current to the final states such that the remaining distance toward a target is zero or minimum at every guidance cycle. The computational process is divided into prediction and correction steps. At the prediction step, an entry trajectory from the current energy state, e_0, to the given final energy state, e_f, is propagated using the parameterized bank angle profile, which is given as a linear function of e as

$$\sigma_{cmd} = \sigma_0 + \frac{e - e_0}{e_f - e_0}(\sigma_f - \sigma_0) \tag{17}$$

where σ_{cmd} is the bank angle command to be applied to the entry dynamics, σ_0 is a positive bank angle to be decided through iterative prediction and correction steps, and σ_f is a pre-selected constant that affects the overall guidance performance. Note that σ_f can be selected to be a small positive number to prevent too much energy dissipation rate. After the prediction step, the correction step is carried out iteratively until the bank angle command profile σ_{cmd} results in a trajectory that satisfies the following terminal range error condition:

$$z(\sigma_0) = s(e_f) - s_f = 0 \tag{18}$$

where $s(e_f)$ is the actual distance traveled, which is a function of σ_{cmd} and is obtained by integrating Eq. (4), and $s_f = s_{go} = R_{go}$ is the range-to-go to the target site at the current guidance cycle. Hence, the terminal range error $z(\sigma_0)$ is a univariate function, the solution of which can be numerically calculated without a burdensome computation process. The computational process employs normalized state variables, where the length is normalized by the Mars radius, the velocity is normalized by the orbital velocity at the Mars radius, and the time is scaled accordingly.

During the prediction and correction process, numerical propagation is performed based on a dimensionless energy-like variable e defined as

$$e = \frac{\mu}{r} - \frac{V^2}{2} \equiv -\mathcal{E} \tag{19}$$

where $\mathcal{E}$ is the conventional specific energy. Taking the derivative of e with respect to time and using dr/dt and dV/dt from Eq. (1) results in the following relationship:

$$\dot{e} = DV \tag{20}$$

which indicates that e monotonically increases. Note that energy-based propagation eliminates the need for flight time information but necessitates the use of final values for altitude and velocity to define the endpoint. Since flight time is not a critical consideration for most entry applications and energy conditions at both ends are often predefined, the LNPCG algorithm can effectively utilize such energy-domain propagation. However, this technique may pose an issue regarding the satisfaction of final conditions. Because energy is a function of altitude and velocity, multiple combinations of altitude and velocity can yield the same energy value [41]. Without an enforcement algorithm for the final altitude or velocity, the final state may not satisfy the desired final condition.

The Newton-Raphson method is employed to find σ_0 satisfying Eq. (18). For a given initial guess of $\sigma_0^{(0)}$ and the current energy state e_0, the kth update for $\sigma_0^{(k)}$ is performed as

$$\sigma_0^{(k+1)} = \sigma_0^{(k)} - \frac{z(\sigma_0^{(k)})}{\partial z(\sigma_0^{(k)})/\partial \sigma_0} \tag{21}$$

where the partial derivative of Eq. (18) with respect to σ_0 is computed by the centered finite difference approximation with a given small increment $\Delta\sigma$ as

$$\frac{\partial z(\sigma_0^{(k)})}{\partial \sigma_0} \approx \frac{z(\sigma_0^{(k)} + \Delta\sigma) - z(\sigma_0^{(k)} - \Delta\sigma)}{2\Delta\sigma} \tag{22}$$

The corrective update continues until the absolute value of Eq. (18) becomes less than a small positive number ϵ. In this study, ϵ and the initial guess for σ_0 are set to one hundred meters and 100 degrees.

3.2. Predictive lateral guidance

Note that all simulations presented in this paper utilize the predictive lateral guidance method proposed in Ref. [42] to achieve high-precision landing accuracy. The method assumes that the computed bank angle from the NPCG algorithm is available for final crossrange computations. The two final crossrange values of the entry trajectory for the converged bank command, which is set to be either positive or negative throughout the entire trajectory, are then determined. If the ratio between two crossrange values exceeds a certain threshold, then a bank reversal occurs. That ratio is set to seven for all simulation results presented in this paper. Note that the initial bank angle direction is determined as the opposite direction to the heading angle error, which can be computed using Eq. (11).

3.3. Final bank angle analysis

In the LNPCG algorithm, σ_f is a design parameter empirically determined by the user to adjust the guidance performance, and Ref. [23] suggests a range of σ_f values to be selected.

Fig. 3 illustrates the trend of entry trajectories depending on σ_f when the LNPCG is employed to solve the human Mars entry mission. All trajectories achieve a targeting accuracy of less than one kilometer, and only their longitudinal quantities and the magnitude of the bank angle are presented. A smaller σ_f results in a larger bank angle in the early phase because the algorithm aims to meet the final range constraint with a given specific energy by modulating σ_0. The entry trajectory with $\sigma_f = 10$ deg (solid blue lines) exhibits the fastest energy dissipation rate, leading to higher peak levels of the path constraints. Interestingly, these

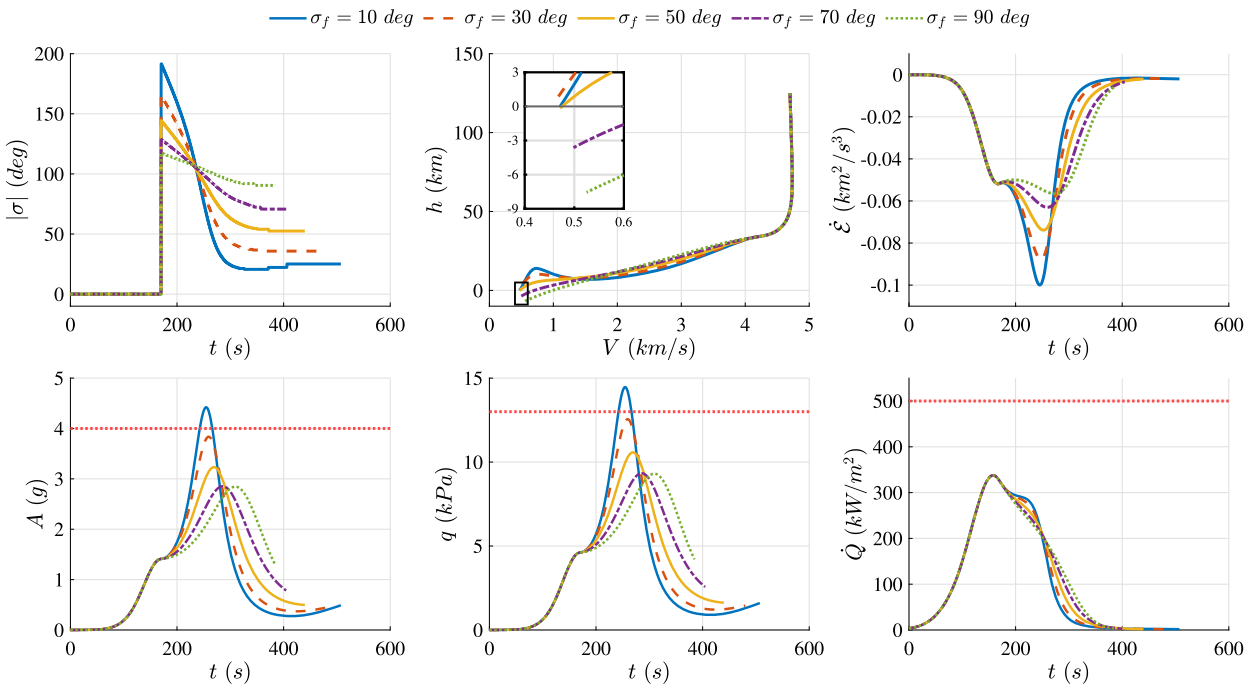

Fig. 3. The influence of σ_f on the LNPCG performance. (For interpretation of the colors in the figure(s), the reader is referred to the web version of this article.)

variations have a more significant impact on the g-load and dynamic pressure profiles rather than the heating rate profile.

Energy dissipation rates also influence the final altitudes. There exists an altitude limit that cannot be further increased through the modulation of σ_f. As shown in the top middle in Fig. 3, the highest altitude reaches 700 meters above the ground with $\sigma_f = 30$ deg. Although the entry trajectory with $\sigma_f = 10$ deg has the slowest energy dissipation rate and altitude rise in the later phase, it dissipates too much energy during the flight, preventing it from reaching high altitudes. On the other hand, a σ_f value of 30 degrees strikes a balance between the early and late phases such that it achieves the highest altitude while satisfying the path constraints.

Entry trajectory should meet a desired final state and path constraints to secure the EDL phase's success. However, modulating σ_f in the LNPCG algorithm doesn't provide sufficient flexibility to design entry trajectories as users desire.

3.4. Guidance activation point analysis

At high altitudes, bank angle modulation has no effect on the entry vehicle's motion due to the absence of aerodynamic forces. We assume the entry vehicle maintains a bank angle command of zero before the guidance law activation. Once the guidance law is activated, the entry vehicle begins to bank and navigate toward the target along a path that satisfies the final range and path constraints with the specific energy at that point. If the energy state at the guidance activation varies, we can anticipate variations in guidance performance.

It is a common practice to use a g-load threshold for entry guidance system activation; for example, 0.15 g is utilized in Ref. [26]. In this paper, however, we adopt the elapsed time from the entry interface, denoting the time at guidance activation as t_{ga}. In Fig. 3, we used $t_{ga} =$ 170 sec.

Fig. 4 illustrates the impact of t_{ga} on guidance performance with σ_f = 40 deg. The LNPCG continues to satisfy the final range constraint even when the guidance law is activated sufficiently after sensible aerodynamic forces are detected. First, it can be observed that the later the guidance law activation, the larger the initial bank angle becomes. This is because delayed guidance law activation implies that the entry vehicle must dissipate more energy than earlier activation before reaching the target. Consequently, the LNPCG algorithm generates a larger bank angle command. On the other hand, earlier guidance law activation results in a faster energy dissipation rate and a higher path constraint peak despite a smaller initial bank angle magnitude.

When the activation of the guidance law is delayed, even beyond the first g-load peak, the entry trajectory achieves an altitude of one kilometer above the ground (see dotted green line in Fig. 4). However, in this specific scenario, especially for mid or high-L/D ratio entry vehicles, excessive delay in activating the guidance law may lead to the entry vehicle skipping out of the atmosphere, resulting in a mission failure. It is crucial to judiciously determine the value of t_{ga} by considering the balance between the conservation of energy in the early phase and the skip-out boundary. A guideline to decide a good t_{ga} is suggested in Section 4.

3.5. A reference design for the human Mars landing mission

In the previous subsections, it was shown that σ_f and t_{ga} significantly affect the guidance performance. By exploring various combinations of σ_f and t_{ga}, we found the best performance achievable using the LNPCG, as shown in Fig. 5. The entry trajectory resulting from the combination of $\sigma_f = 40$ deg and $t_{ga} = 175$ sec achieves the highest final altitude exceeding one kilometer and satisfies the path constraints having approximately 10% margins in g-load and dynamic pressure.

Despite the predefined final altitude and velocity values of 2.48 km and 450 m/s, respectively, the entry trajectory generated by the LNPCG ends with a final state of 1.04 km and 461 m/s. This discrepancy is attributed to the baseline NPCG algorithm that aims to satisfy only the range constraint at a specific final energy condition. Accordingly, multiple combinations of altitude and velocity can exist for the same energy value. More importantly, the linear bank angle parameterization fails to preserve sufficient energy margins toward the end of entry trajectories so that the final state condition cannot be satisfied. As demonstrated in Fig. 5, the LNPCG has some limitations to be applied to the human Mars landing mission.

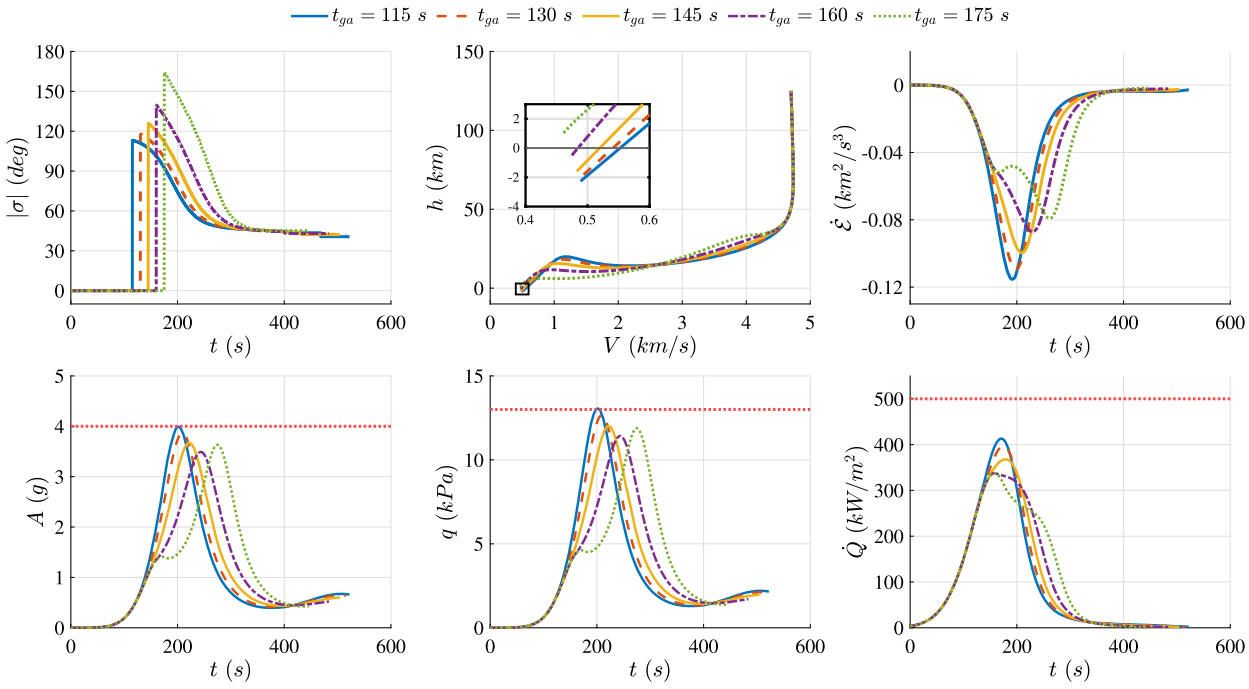

Fig. 4. The influence of guidance law activation point on the LNPCG performance.

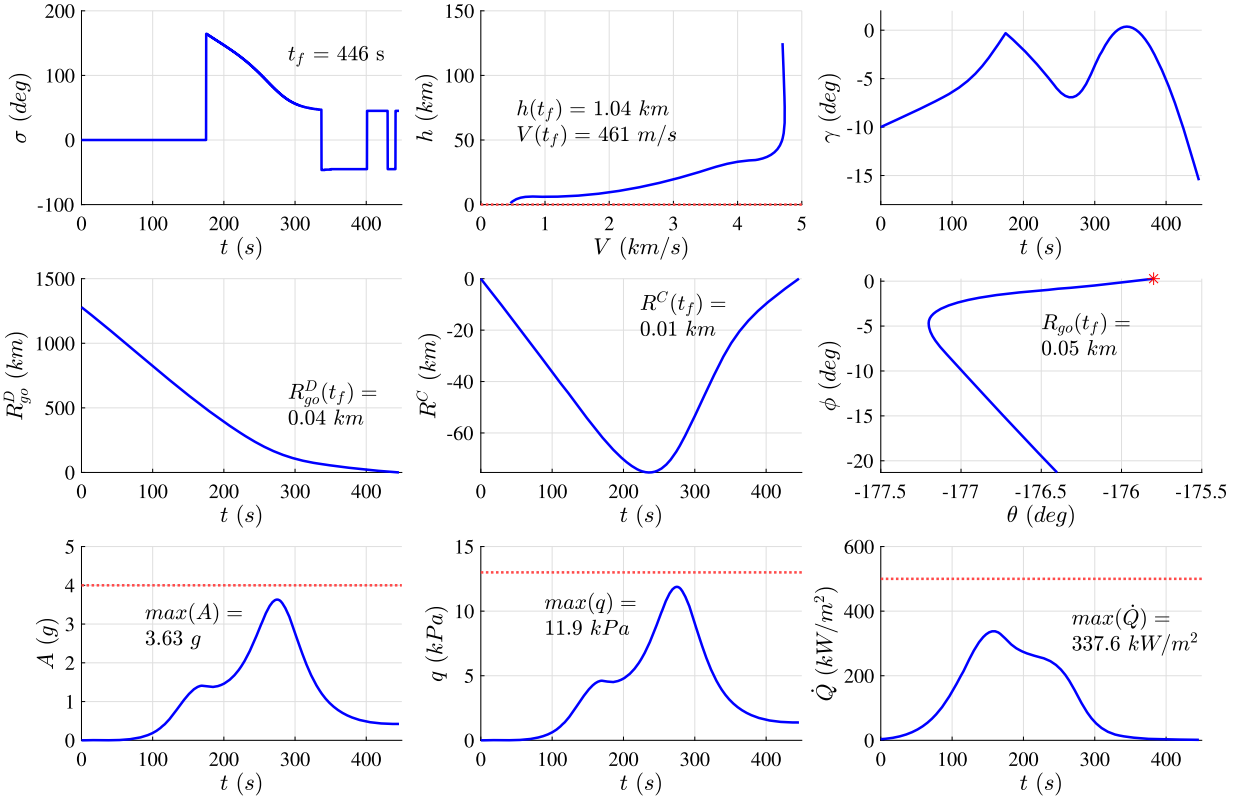

Fig. 5. Among the entry trajectories generated using the LNPCG, the one path that possesses the highest altitude while satisfying the path constraints.

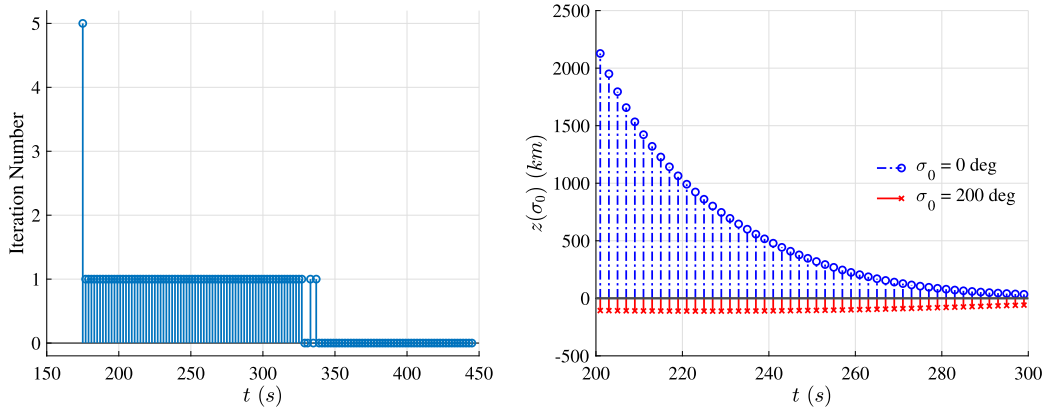

Fig. 6. Left: the number of iterations required to find a solution at each guidance cycle. Right: the extreme overshoot and undershoot profiles with $\sigma_0 = 0$ and 200 deg input.

3.6. Convergence analysis

It has been known that the NPCG algorithm requires substantial onboard computational power, especially for long-range flights, and lacks theoretical convergence guarantees [43,44]. The left side of Fig. 6, however, demonstrates the computational effectiveness of the NPCG algorithm. It displays the number of iterations required to converge at each guidance cycle. For all cycles after the first one, only one or less iteration was needed to find a solution. This is because the initial guess for the next step is based on the previous step's solution, and their values should be similar, so multiple iterations are unnecessary.

The right side of Fig. 6 confirms the existence of a solution that satisfies the final range constraint along the entry trajectory. Only a part of the entry trajectory spanning from 200 to 300 seconds is shown for better readability. The blue and red vertical lines with dots indicate overshoot and undershoot distances using a certain σ_0, respectively. Having opposite signs for extreme overshoot and undershoot values implies a solution of Eq. (18) must exist, according to Bolzano's theorem [45], a special case of the intermediate value theorem.

Intuitively, the maximum overshoot distance is obtained with a σ_0 value of zero, which means that the entry vehicle flies mostly in the full lift-up mode. On the other hand, the minimum undershoot distance is obtained around σ_0 of 200 deg rather than 180 deg, and this value may change depending on the mission condition and bank angle parameterization. This analysis is used as a stopping criterion for the NPCG algorithm:

$$z(0\ deg) \cdot z(200\ deg) > 0 \tag{23}$$

where the terminal range error $z(\sigma_0)$ is defined by Eq. (18). Satisfying Eq. (23) indicates that a solution does not exist at that guidance cycle, and there is no need to continue the solution-finding process. Therefore, if the stopping criterion is satisfied, then the NPC process terminates, and the guidance system retains the σ_0 solution from the previous cycle.

As the entry vehicle approaches the target closely, the extreme overshoot and undershoot values may no longer have opposite signs. It was observed that this additional stopping criterion helped the NPCG algorithm avoid convergence issues effectively when dispersions and randomnesses were included in the simulations (i.e., the Monte Carlo simulations presented in Subsection 4.4).

4. Autonomous numerical predictor-corrector guidance (ANPCG)

Section 3 highlighted the limited capabilities of the LNPCG in that it cannot meet the final altitude requirement of the human Mars entry mission. This limitation is attributed to the linear bank profile not preserving sufficient energy toward the end of the entry trajectory. To address this issue, we propose enhancing the energy preservation capability by substituting the linear bank angle with a novel bank profile. In addition, a guideline to decide the guidance activation time that can maximize energy preservation in the early entry phase is suggested.

4.1. Guidance activation point determination

In Ref. [19], a controllability test was conducted to determine the point at which bank control begins to affect the entry vehicle's motion. This study aims to take a step further by selecting the ideal guidance law activation point that enhances the entry guidance performance, as depicted in Fig. 4. To meet the final range constraint and dissipate the provided specific energy, it is essential to decide wisely the guidance activation time to achieve the entry guidance goal.

Fig. 7 illustrates the entry trajectory in which a full lift-up command is given for a sufficient duration, resulting in a skip-out at the end. Even though the entry vehicle is in the moment of skipping out, it will eventually re-enter the Martian atmosphere and land on the ground if it continues flying. The maximum g-load of 1.41 g and the minimum altitude of 34 km occur at 170.5 seconds and 177.8 seconds, respectively, denoted as red and green asterisks. The entry vehicle experiences the peak g-load shortly before reaching its lowest altitude due to the fact that the g-load has a proportional relationship to air density times velocity squared (Eq. (5a)).

The specific energy will dissipate at a minimum rate during the full lift-up flight. On the other hand, activating the guidance law after passing the minimum altitude can result in preserving excessive energy for a given range-to-go so that the NPCG algorithm cannot find a solution. Therefore, we determine that the proposed entry guidance should be activated strategically between the point of maximum g-load and the minimum altitude. This approach allows the entry vehicle to preserve sufficient energy during the early phase and eventually increase the potential final altitude and decrease the path constraints peaks. We adopt a fixed t_{ga} value of 175 seconds for the proposed guidance method.

4.2. Logistic function-based bank angle parameterization

We propose a novel bank angle parameterization utilizing a logistic function, a type of sigmoid function, to enhance the mitigation of energy dissipation during the early entry phase and potentially achieve higher final altitudes, as follows:

$$\sigma_{cmd} = \frac{2\sigma_0}{1 + \exp\left[K(e - e_0)/(e_f - e_0)\right]} \tag{24}$$

where the parameter K represents the decay rate, adjusting how quickly the bank angle reduces. Note that σ_{cmd} at e_0 is σ_0 regardless of K, whereas σ_{cmd} at e_f is affected by K.

Fig. 8 illustrates the trend of entry trajectories varying with respect to K. The guidance activation time t_{ga} is set to 175 seconds. As ob-

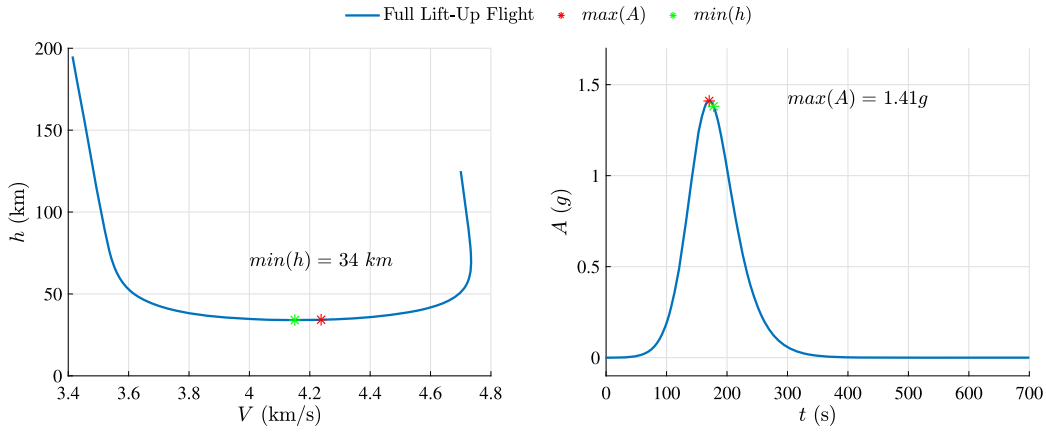

Fig. 7. The entry trajectory with a full lift-up command maintained for 700 seconds. Left: velocity versus altitude profile. Right: g-load profile.

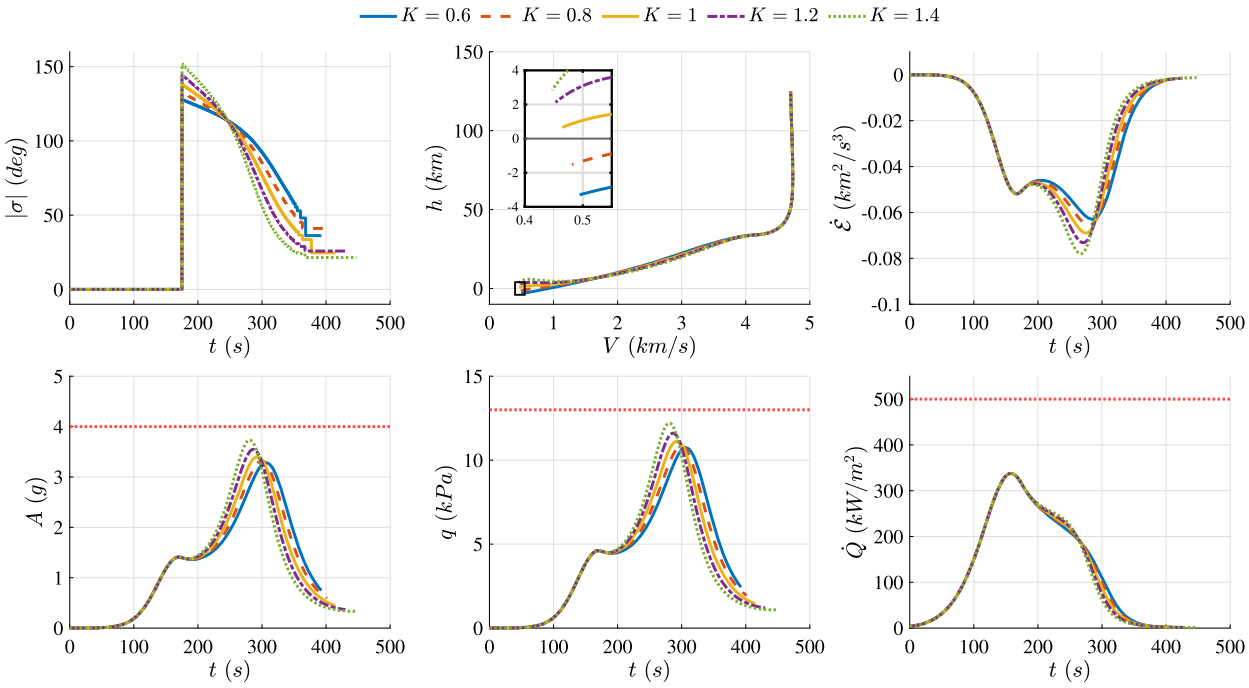

Fig. 8. The trend of entry trajectories varying with respect to the decay rate K variations.

served, a larger value of K causes the bank angle profile in the early stage to steepen, leading to a higher rate of energy dissipation and an increase in the peaks of path constraints. Moreover, a higher value of K results in a lower magnitude of the bank angle in the later stage, thereby increasing the final altitude of the entry trajectory. When K is set to 1.4, the highest altitude achieved is 2.85 km, which is higher than the required altitude of 2.48 km. This indicates that the proposed guidance method is effective in mitigating the energy dissipation rate and increasing the final altitudes. However, similar to the case of LNPCG, there exists an altitude limit that cannot be increased by adjusting K. The decay rate that satisfies the mission requirement is found to be 1.28, and the corresponding simulation result is presented in Fig. 9.

4.3. Comparison analysis

The comparison between the LNPCG and ANPCG entry trajectories is illustrated in Fig. 10 that overlaps Figs. 5 and 9. As can be seen from the top left in Fig. 10, the bank angle magnitude of the ANPCG is lower than that of the LNPCG in both the early and late phases, whereas it is reversed in the middle. At the time when guidance is activated, the bank angle magnitudes are 164 and 147 degrees for each method, and this results in the ANPCG trajectory having a 15% larger vertical lift component compared to the LNPCG. The LNPCG's 164-degree bank angle represents an almost full lift-down maneuver, causing the entry vehicle to quickly decelerate. The difference in bank angle commands is accumulated over time, and this effect leads to the ANPCG having a 6% slower energy dissipation rate than the LNPCG when their peak values are compared. As a result, the proposed guidance algorithm effectively reduces the energy dissipation rate in the early phase, allowing the ANPCG to reach a 1.4 km higher altitude and end with an 11.7 m/s lower velocity compared to the LNPCG's best performance. The peak path constraint values remain similar for both guidance methods.

Fig. 11 presents the bank command profiles plotted every 10^{th} guidance cycle in the energy domain for the entry trajectories previously shown in Fig. 10. e_{ga} is the energy state at the guidance activation point. The respective bank profiles starting with σ_0 are sought by the NPC technique such that the bank profiles satisfy the final range constraint at each guidance. The left side of Fig. 11 presents the bank command

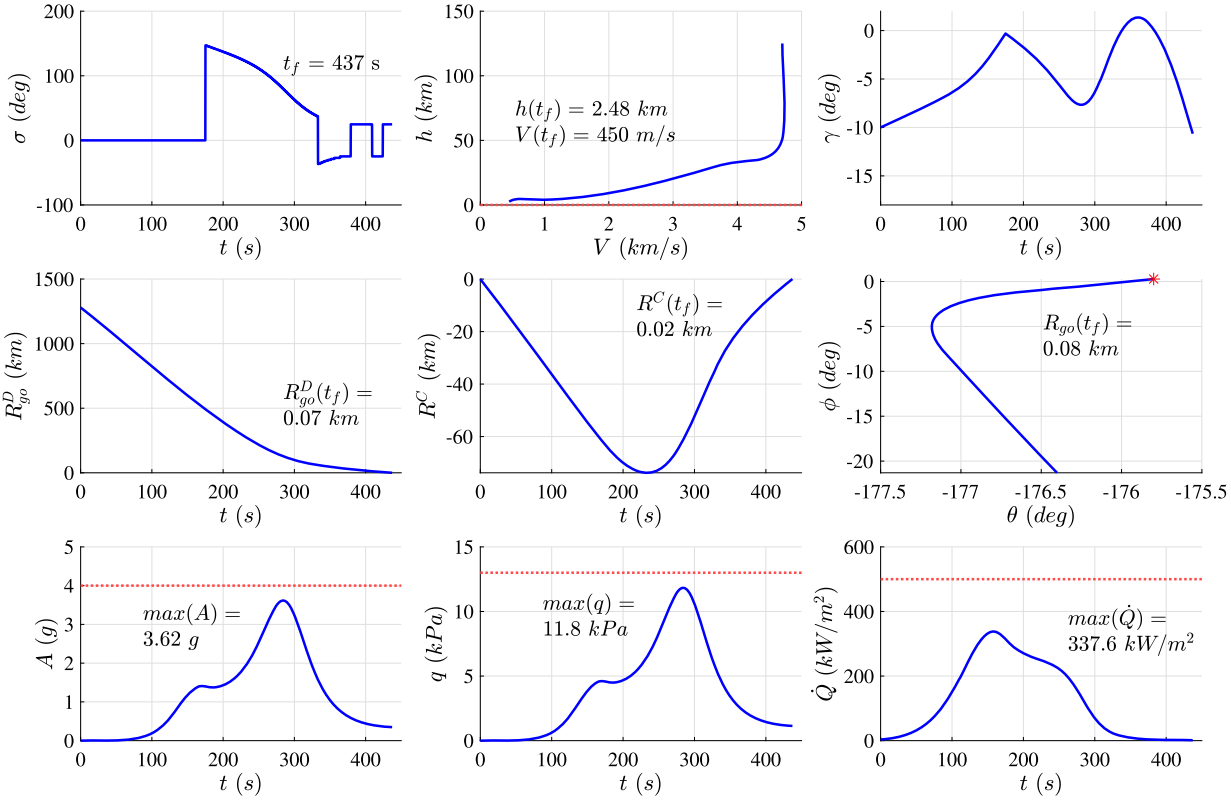

Fig. 9. The entry trajectory generated by the ANPCG when $K = 1.28$ and $t_{ga} = 175$ sec.

Table 2
Dispersion levels on the entry interface and models.

Parameters	Three-Standard Deviation Distributions [16]
r	100 m
θ	0.25 deg
ϕ	0.25 deg
V	3.3 m/s
γ	0.1 deg
ψ	0.17 deg
m	200 kg
ρ	5%

profiles of the LNPCG, which appears to be linear. Towards the end of the trajectory, as the remaining crossrange error becomes comparable to the downrange-to-go, σ_0 starts deviating from its linear profile. This is because the baseline NPCG algorithm is designed to manage the range-to-go, which is a combination of crossrange and downrange-to-go.

The bank command profiles of the ANPCG exhibit a unique attribute as they vary the final bank angle at each guidance cycle, unlike the LNPCG. Based on the computed σ_0 value, the final bank angle is automatically determined, resulting in better energy management. The final bank angle of the algorithm is adjusted from large to small values so that it can have a lower energy dissipation rate in the early phase and eventually achieve a higher altitude at the end. For the LNPCG, if a small final bank angle is chosen to obtain a high final altitude (see Fig. 3), it demands a large initial bank angle to satisfy the range constraint, which eventually causes an excessive energy dissipation rate at the early phase.

The ANPCG algorithm possesses almost identical convergence features as that of the LNPCG (see Fig. 6). The effectiveness and the guarantee of the solution's existence are still valid for the ANPCG algorithm because both methods are rooted in the NPC targeting guidance algorithm.

4.4. Monte Carlo simulation

The Monte Carlo method is adopted to examine the effect of entry interface dispersion and modeling errors on the guidance performance. The entry interface is randomly sampled from a Gaussian distribution with three standard deviations, and they are given in Table 2. The dispersion levels are adopted from Ref. [16]. A 1000-run Monte Carlo simulation is conducted for each guidance method.

Fig. 12 presents the results of Monte Carlo simulations conducted to compare the performance of the LNPCG and ANPCG. Table 3 summarizes the statistical data; the mean (M), median (Mdn), and standard deviation (SD) of the final miss distance ($R_{go}(t_f)$), final altitude ($h(t_f)$), and final velocity ($V(t_f)$). The results show that the baseline NPCG algorithm is highly robust against random distributions and can successfully meet the final range constraint. This is evident from the left side of Fig. 12, where 100% of the entry trajectories generated by both methods arrive within a one-kilometer boundary from the landing point. Although the mean miss distance of the LNPCG is lower than the ANPCG by about a hundred meters, 166 meters versus 273 meters, this difference is negligible considering the final miss distance requirement, which is less than five kilometers.

The right side of Fig. 12 clearly illustrates the difference between the LNPCG and ANPCG in achieving the desired final altitude and velocity represented in dotted lines ($h_t = 2480$ m and $V_t = 450$ m/s). It should be noted that the mean final altitude and velocity achieved by the ANPCG implementation are very close to the mission requirement, with less than 0.3% errors. The mean final altitude ($M[h(t_f)]$) of the LNPCG is about 1.4 km lower than that of the ANPCG, and this causes the higher mean final velocity ($V[h(t_f)]$) because the NPCG algorithm terminates at the predetermined final energy value. The difference in the mean final velocity is 12 m/s, which may lead to significantly increased fuel consumption during the following powered descent landing phase due to the heaviness of the entry vehicle. Fig. 13 shows the histogram of the

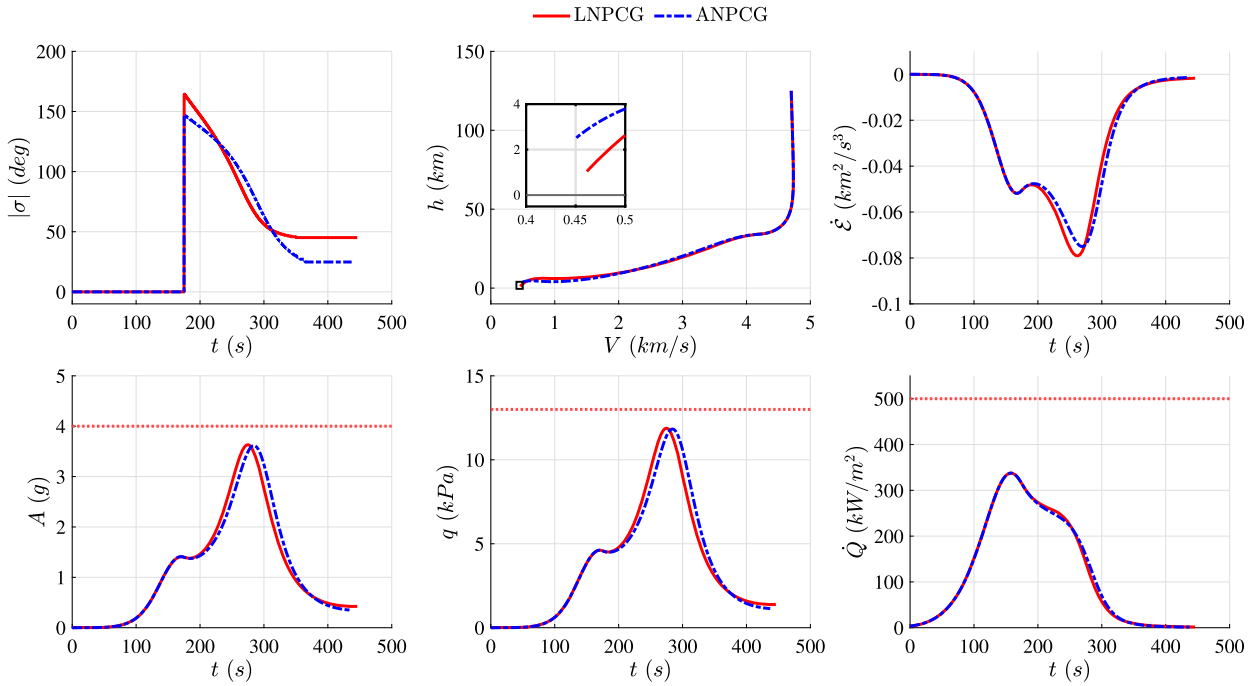

Fig. 10. Comparison between the entry trajectories generated by the LNPCG and ANPCG. Only the longitudinal quantities are presented.

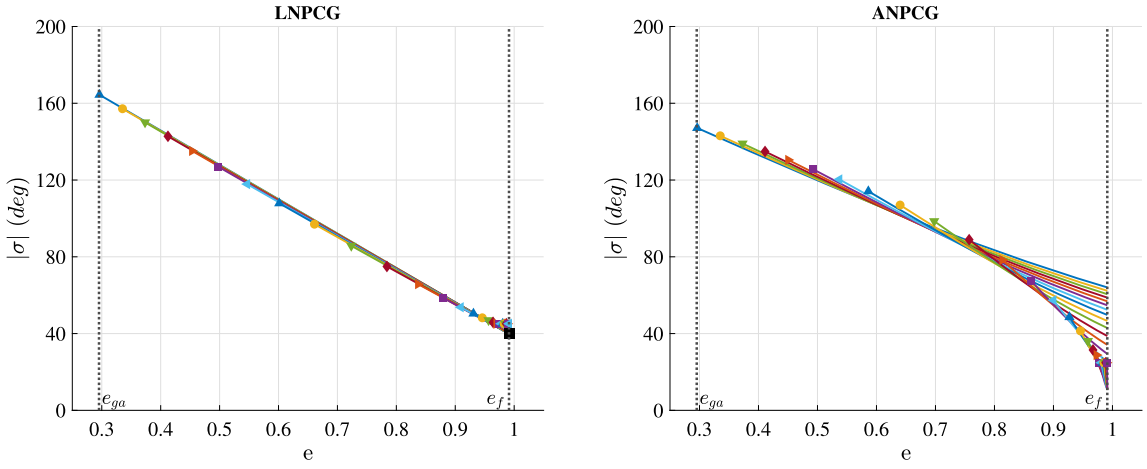

Fig. 11. The bank command profiles plotted every 10^{th} guidance cycle in the energy domain. Left: the linear bank angle profiles of the LNPCG. Right: the logistic bank angle profiles of the ANPCG.

final altitude and velocity of each method. As evidently seen from the histogram, the entry trajectories of the ANPCG arrive much closer to the mission requirement compared to those of the LNPCG. Since the modeling randomness and dispersions used in the Monte Carlo simulations were symmetrically distributed, we can expect the mean and median values of the dataset to be similar. Table 3 provides evidence of this.

Note that there is no instance where path constraints are violated by both methods. Furthermore, there are no significant disparities in peak values of path constraints between the two guidance methods, as displayed in Fig. 10. However, path constraint handling is an imperative task in entry guidance, and this will be addressed in future work.

5. Conclusion and future work

This paper has demonstrated the limitations of the existing entry guidance method and proposed a new approach for a future human Mars landing mission. Simulation analysis has revealed that the LNPCG causes excessive energy dissipation rates during the early entry phase, leading to failure to meet the final state condition. By introducing a novel bank angle parameterization and adjusting the guidance law activation point, the ANPCG provides improved guidance performance with higher final altitudes and lower final velocities. The analysis result has suggested that the proposed guidance can be a more suitable option for future atmospheric entry missions.

The proposed method has the potential for further improvement through various research avenues. Currently, achieving satisfactory guidance performance requires a manual selection of guidance parameters. The method could be fully automated by adaptively determining guidance parameters based on vehicle states and conditions [46,47]. The simulation results presented here assume perfect navigation and attitude control. Incorporating sensor noise [48,49] and attitude dynamics [50,51] into the algorithm and simulation environment would rigorously demonstrate the proposed method's performance. Furthermore, the current method only constrains a final range such that final altitude and velocity sets have large distributions. If the bank angle parameterization within the algorithm is more flexible, for example, using a

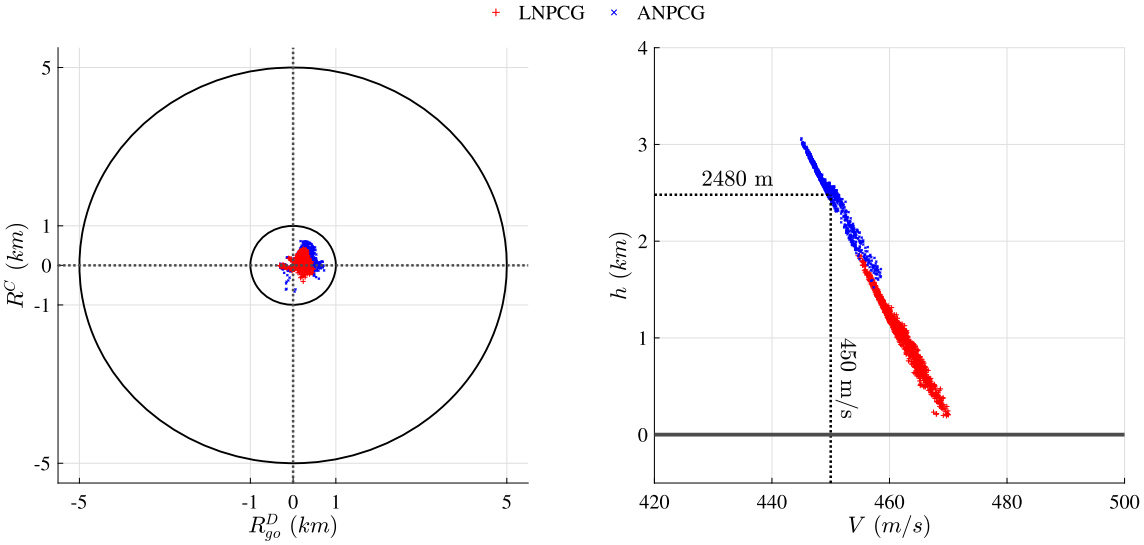

Fig. 12. The terminal state dispersions of entry trajectories of the LNPCG and ANPCG. Left: the final miss distance, right: the final altitude and velocity.

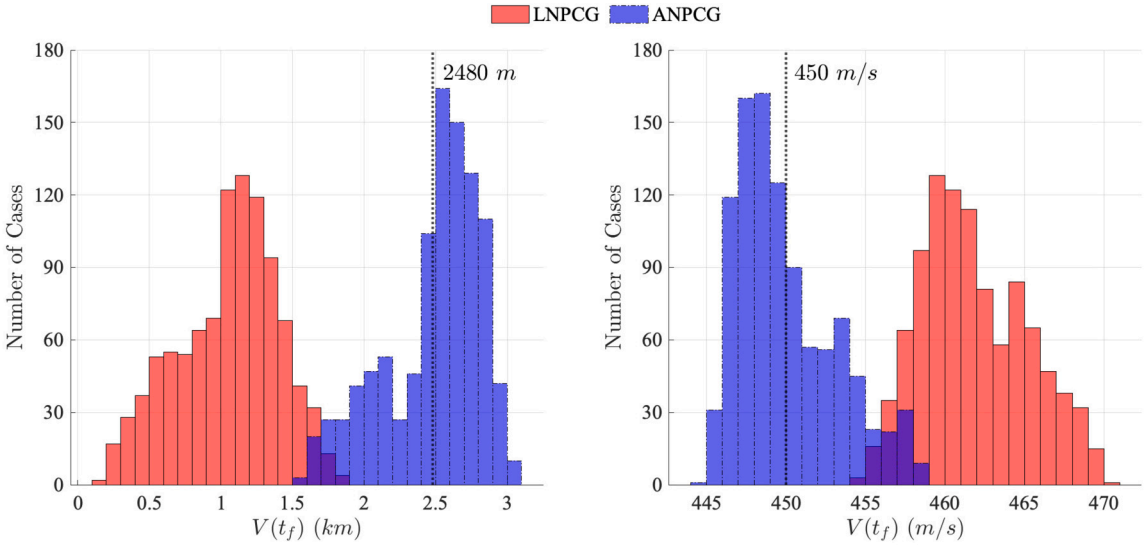

Fig. 13. The terminal state dispersions of entry trajectories of the LNPCG and ANPCG. Left: the final miss distance, right: the final altitude and velocity.

Table 3
The statistics of the Monte Carlo simulation results: M, Mdn, and SD are mean, median, and standard deviation operators, respectively.

Statistics	LNPCG	ANPCG	Statistics	LNPCG	ANPCG
$M[R_{go}(t_f)]$	166 m	273 m	$M[max(A)]$	3.6 g	3.6 g
$Mdn[R_{go}(t_f)]$	90 m	246 m	$Mdn[max(A)]$	3.6 g	3.6 g
$SD[R_{go}(t_f)]$	130 m	208 m	$SD[max(A)]$	0.1 g	0.1 g
$M[h(t_f)]$	1052 m	2487 m	$M[max(q)]$	11.9 kPa	11.9 kPa
$Mdn[h(t_f)]$	1049 m	2562 m	$Mdn[max(q)]$	11.9 kPa	11.9 kPa
$SD[h(t_f)]$	355 m	334 m	$SD[max(q)]$	0.3 kPa	0.3 kPa
$M[V(t_f)]$	462 m/s	450 m/s	$M[max(\dot{Q})]$	337.5 kW/m^2	337.6 kW/m^2
$Mdn[V(t_f)]$	461 m/s	449 m/s	$Mdn[max(\dot{Q})]$	337.3 kW/m^2	337.7 kW/m^2
$SD[V(t_f)]$	3 m/s	3 m/s	$SD[max(\dot{Q})]$	3.0 kW/m^2	2.9 kW/m^2

quadratic profile as in Ref. [52], it will allow for direct control of other constraints, such as final altitude or velocity, to be achieved simultaneously. Lastly, the potential applications of entry guidance for planetary landing missions could be expanded. Incorporating waypoint and no-fly zone algorithms [53,54] into the proposed method could be utilized for hypersonic gliding vehicles and reusable rocket entry guidance.

CRediT authorship contribution statement

Youngro Lee: Writing – original draft, Validation, Software, Methodology, Investigation, Formal analysis. **David D. Lee:** Writing – original draft, Supervision, Funding acquisition, Formal analysis. **Bong Wie:** Writing – original draft, Supervision, Software.

Declaration of competing interest

The authors declare the following financial interests/personal relationships which may be considered as potential competing interests: Dae Young Lee reports financial support was provided by National Science Foundation. If there are other authors, they declare that they have no known competing financial interests or personal relationships that could have appeared to influence the work reported in this paper.

Acknowledgements

The authors would like to express special thanks to Dr. Aaron Brandis of NASA Ames Research Center for sharing his knowledge for the research described in this paper. This work was also partially supported by the National Science Foundation through award 2327379. We thank NSF's EPSCoR program director, Pinhas Ben-Tzvi.

Data availability

No data was used for the research described in the article.

References

[1] C.A. Kluever, Entry guidance performance for Mars precision landing, J. Guid. Control Dyn. 31 (2008) 1537–1544, https://doi.org/10.2514/1.36950.
[2] R. Powell, Numerical roll reversal predictor corrector aerocapture and precision landing guidance algorithms for the Mars surveyor program 2001 missions, in: 23rd Atmospheric Flight Mechanics Conference, 1998.
[3] P. Lu, S. Forbes, M. Baldwin, Gliding guidance of high l/d hypersonic vehicles, in: AIAA Guidance, Navigation, and Control (GNC) Conference, 2013.
[4] R. Chowdhry, C. Zimmermann, H. Youssef, H. Lee, P. Rodi, Predictor-corrector entry guidance for reusable launch vehicles, in: AIAA Guidance, Navigation, and Control Conference and Exhibit, 2001.
[5] S. Striepe, E. Queen, R. Powell, R. Braun, F. Cheatwood, J. Aguirre, L. Sachi, D. Lyons, An atmospheric guidance algorithm testbed for the Mars surveyor program 2001 orbiter and lander, in: 23rd Atmospheric Flight Mechanics Conference, 1998.
[6] M.R. Grover, B.D. Cichy, P.N. Desai, Overview of the Phoenix entry, descent, and landing system architecture, J. Spacecr. Rockets 48 (2011) 706–712, https://doi.org/10.2514/1.46548.
[7] G.F. Mendeck, L. Craig McGrew, Entry guidance design and postflight performance for 2011 Mars science laboratory mission, J. Spacecr. Rockets 51 (2014) 1094–1105, https://doi.org/10.2514/1.A32737.
[8] S. Dutta, C.D. Karlgaard, D. Kass, G. Villar, M. Mischna, Post-flight analysis of atmospheric properties from Mars 2020 entry, descent, and landing, in: AIAA SCITECH 2022 Forum, 2022.
[9] C.A. Graves, J.C. Harpold, Apollo Experience Report: Mission Planning for Apollo Entry, Technical Report, NASA TN-D-6725, 1972.
[10] R.A. Lugo, R. Powell, A.M. Dwyer-Cianciolo, Overview of a generalized numerical predictor-corrector targeting guidance with application to human-scale Mars entry, descent, and landing, in: AIAA Scitech 2020 Forum, 2020.
[11] B.J. Johnson, P. Lu, C. Cerimele, Mid-lift-to-drag ratio rigid vehicle 6-dof edl performance using tunable Apollo powered guidance, in: AAS/AIAA Space Flight Mechanics Meeting, 2019, https://ntrs.nasa.gov/citations/20200001595.
[12] G. Mendeck, L. Craig, Entry guidance for the 2011 Mars science laboratory mission, in: AIAA Atmospheric Flight Mechanics Conference, 2011.
[13] J. Benito, K. Mease, Entry trajectory planning for higher elevation landing, in: Advances in the Astronautical Sciences 07-309, 2007, pp. 939–958.
[14] P.N. Desai, P.C. Knocke, Mars exploration rovers entry, descent, and landing trajectory analysis, J. Astronaut. Sci. 55 (2007) 311–323, https://doi.org/10.1007/BF03256527.
[15] R.D. Braun, R.M. Manning, Mars exploration entry, descent, and landing challenges, J. Spacecr. Rockets 44 (2007) 310–323, https://doi.org/10.2514/1.25116.
[16] B.J. Johnson, P. Lu, R.R. Sostaric, Mid lift-to-drag rigid vehicle 6-dof performance for human Mars entry, descent, and landing: a fractional polynomial powered descent guidance approach, in: AIAA Scitech 2020 Forum, 2020.
[17] B.J. Johnson, C.J. Cerimele, S. Stachowiak, R.R. Sostaric, D.A. Matz, P. Lu, Mid-lift-to-drag ratio rigid vehicle control system design and simulation for human Mars entry, in: 2018 AIAA Guidance, Navigation, and Control Conference, 2018.
[18] Y. Lee, D.Y. Lee, B. Wie, A comparative study of entry guidance for Mars robotic and human landing missions, Acta Astronaut. 215 (2024) 178–193, https://doi.org/10.1016/j.actaastro.2023.11.045.
[19] Y. Lee, D.Y. Lee, Entry trajectory generation for Mars robotic and human missions based on a predetermined bank angle profile, Adv. Space Res. 71 (2023) 3301–3312, https://doi.org/10.1016/j.asr.2022.12.021.
[20] J.L. DiCarlo, Aerocapture Guidance Methods for High Energy Trajectories, Ph.D. thesis, Massachusetts Institute of Technology, 2003.
[21] C. Zimmerman, G. Dukeman, J. Hanson, Automated method to compute orbital reentry trajectories with heating constraints, J. Guid. Control Dyn. 26 (2003) 523–529, https://doi.org/10.2514/2.5096.
[22] A. Joshi, K. Sivan, S.S. Amma, Predictor-corrector reentry guidance algorithm with path constraints for atmospheric entry vehicles, J. Guid. Control Dyn. 30 (2007) 1307–1318, https://doi.org/10.2514/1.26306.
[23] P. Lu, Predictor-corrector entry guidance for low-lifting vehicles, J. Guid. Control Dyn. 31 (2008) 1067–1075, https://doi.org/10.2514/1.32055.
[24] S. Xue, P. Lu, Constrained predictor-corrector entry guidance, J. Guid. Control Dyn. 33 (2010) 1273–1281, https://doi.org/10.2514/1.49557.
[25] C.W. Brunner, P. Lu, Comparison of fully numerical predictor-corrector and Apollo skip entry guidance algorithms, J. Astronaut. Sci. 59 (2012) 517–540, https://doi.org/10.1007/S40295-014-0005-1.
[26] P. Lu, Entry guidance: a unified method, J. Guid. Control Dyn. 37 (2014) 713–728, https://doi.org/10.2514/1.62605.
[27] P. Lu, C.W. Brunner, S.J. Stachowiak, G.F. Mendeck, M.A. Tigges, C.J. Cerimele, Verification of a fully numerical entry guidance algorithm, J. Guid. Control Dyn. 40 (2017) 230–247, https://doi.org/10.2514/1.G000327.
[28] Z. Liang, S. Zhu, Constrained predictor-corrector guidance via bank saturation avoidance for low l/d entry vehicles, Aerosp. Sci. Technol. 109 (2021) 106448, https://doi.org/10.1016/j.ast.2020.106448.
[29] B. Zhang, S. Tang, B. Pan, Automatic load relief numerical predictor-corrector guidance for low l/d vehicles return from low earth orbit, Proc. Inst. Mech. Eng., G J. Aerosp. Eng. 229 (2015) 2106–2118, https://doi.org/10.1177/0954410014567157.
[30] W.J. Zhang, B.M. Wang, Predictor corrector algorithms considering multiple constraints for entry vehicles, Aeronaut. J. 126 (2022) 1874–1896, https://doi.org/10.1017/aer.2022.19.
[31] T. Wang, H. Zhang, G. Tang, Predictor-corrector entry guidance with waypoint and no-fly zone constraints, Acta Astronaut. 138 (2017) 10–18, https://doi.org/10.1016/j.actaastro.2017.05.009.
[32] R. Furfaro, D. Wibben, Mars atmospheric entry guidance via multiple sliding surface guidance for reference trajectory tracking, in: AIAA/AAS Astrodynamics Specialist Conference, 2012.
[33] K.D. Webb, P. Lu, Entry guidance by onboard trajectory planning and tracking, in: AIAA Atmospheric Flight Mechanics Conference, 2016.
[34] X. Jiang, S. Li, R. Furfaro, Integrated guidance for Mars entry and powered descent using reinforcement learning and pseudospectral method, Acta Astronaut. 163 (2019) 114–129, https://doi.org/10.1016/j.actaastro.2018.12.033.
[35] M. Sagliano, P. Lu, B. Johnson, D. Seelbinder, S. Theil, Six-degrees-of-freedom aeropropulsive entry trajectory optimization, in: AIAA SCITECH 2024 Forum, 2024.
[36] J.A. Samareh, Parametric trade study of mid lift/drag entry systems for human Mars mission, in: AIAA Scitech 2020 Forum, 2020.
[37] R.R. Sostaric, C.J. Cerimele, E.A. Robertson, J.A. Garcia, A rigid mid lift-to-drag ratio approach to human Mars entry, descent, and landing, in: 2017 AIAA Guidance, Navigation, and Control Conference, 2017.
[38] Y. Gong, Y. Guo, G. Ma, M. Guo, Mars entry guidance for mid-lift-to-drag ratio vehicle with control constraints, Aerosp. Sci. Technol. 107 (2020) 106361, https://doi.org/10.1016/j.ast.2020.106361.
[39] B.J. Johnson, E.M. Braden, R.R. Sostaric, C.J. Cerimele, P. Lu, Entry, descent, and landing performance for a mid-lift-to-drag ratio vehicle at Mars, in: 2018 American Astronautical Society Guidance and Control Conference, 2018, https://ntrs.nasa.gov/citations/20180001748.
[40] S.C. Paschall, Mars Entry Navigation Performance Analysis Using Monte Carlo Techniques, Ph.D. thesis, Massachusetts Institute of Technology, Dept. of Aeronautics and Astronautics, 2004, http://hdl.handle.net/1721.1/16661.
[41] P. Lu, S. Sandoval, C. Davami, Fast and robust optimization of full trajectory from entry through powered descent, J. Guid. Control Dyn. 47 (2024) 203–216, https://doi.org/10.2514/1.G007564.
[42] K.M. Smith, Predictive lateral logic for numerical entry guidance algorithms, in: AAS/AIAA Space Flight Mechanics Meeting, JSC-CN-35110-1, 2016.

[43] L. Zang, D. Lin, S. Chen, H. Wang, Y. Ji, An on-line guidance algorithm for high l/d hypersonic reentry vehicles, Aerosp. Sci. Technol. 89 (2019) 150–162, https://doi.org/10.1016/j.ast.2019.03.052.
[44] J. Ridderhof, P. Tsiotras, B.J. Johnson, Stochastic entry guidance, J. Guid. Control Dyn. 45 (2022) 320–334, https://doi.org/10.2514/1.G005964.
[45] S. Russ, A translation of Bolzano's paper on the intermediate value theorem, Hist. Math. 7 (1980) 156–185, https://doi.org/10.1016/0315-0860(80)90036-1.
[46] G. Peng, B. Wang, L. Liu, H. Fan, Z. Cheng, Real-time adaptive entry trajectory generation with modular policy and deep reinforcement learning, Aerosp. Sci. Technol. 142 (2023) 108594, https://doi.org/10.1016/j.ast.2023.108594.
[47] S. Osler, T. Sands, Controlling remotely operated vehicles with deterministic artificial intelligence, Appl. Sci. 12 (2022), https://doi.org/10.3390/app12062810.
[48] J.A. Rataczak, D. Amato, J.W. McMahon, Density estimation for entry guidance problems using deep learning, in: AIAA SCITECH 2024 Forum, 2024.
[49] E. Wilt, T. Sands, Microsatellite uncertainty control using deterministic artificial intelligence, Sensors 22 (2022), https://doi.org/10.3390/s22228723.
[50] A. Vitiello, E.M. Leonardi, M. Pontani, Multiple-sliding-surface guidance and control for terminal atmospheric reentry and precise landing, J. Spacecr. Rockets 60 (2023) 912–923, https://doi.org/10.2514/1.A35438.
[51] A. Sandberg, T. Sands, Autonomous trajectory generation algorithms for spacecraft slew maneuvers, Aerospace 9 (2022), https://doi.org/10.3390/aerospace9030135.
[52] Z. Li, B. He, M. Wang, H. Lin, X. An, Time-coordination entry guidance for multi-hypersonic vehicles, Aerosp. Sci. Technol. 89 (2019) 123–135, https://doi.org/10.1016/j.ast.2019.03.056.
[53] R. Zhang, N. Cui, Entry trajectory optimization with general polygonal no-fly zone constraints, IEEE Trans. Aerosp. Electron. Syst. 59 (2023) 9205–9218, https://doi.org/10.1109/TAES.2023.3319590.
[54] K. Raigoza, T. Sands, Autonomous trajectory generation comparison for de-orbiting with multiple collision avoidance, Sensors 22 (2022), https://doi.org/10.3390/s22187066.